

# Oscillation tomography of the Earth with solar neutrinos and future experiments

P. Bakhti<sup>1</sup> and A.Yu. Smirnov<sup>2,3</sup>

<sup>1</sup> *School of physics, Institute for Research in Fundamental Sciences (IPM),  
P.O.Box 19395-5531, Tehran, Iran*

<sup>2</sup> *Max-Planck Institute for Nuclear Physics,  
Saupfercheckweg 1, D-69117 Heidelberg, Germany*

<sup>3</sup> *ICTP, Strada Costiera 11, 34014 Trieste, Italy*

We study in details the Earth matter effects on the boron neutrinos from the Sun using recently developed 3D models of the Earth. The models have a number of new features of the density profiles, in particular, substantial deviation from spherical symmetry. In this connection we further elaborate on relevant aspects of oscillations ( $\epsilon^2$  corrections, adiabaticity violation, entanglement, *etc.*) and the attenuation effect. The night excesses of the  $\nu e$ - and  $\nu N$ - events and the Day-Night asymmetries,  $A_{ND}$ , are presented in terms of the matter potential and the generalized energy resolution functions. The energy dependences of the cross-section and the flux improve the resolution, and consequently, sensitivity to remote structures of the profiles. The nadir angle ( $\eta$ ) dependences of  $A_{ND}$  are computed for future detectors DUNE, THEIA, Hyper-Kamiokande and MICA at the South pole. Perspectives of the oscillation tomography of the Earth with the boron neutrinos are discussed. Next generation of detectors will establish the integrated day-night asymmetry with high confidence level. They can give some indications of the  $\eta$ -dependence of the effect, but will discriminate among different models at most at the  $(1-2)\sigma$  level. For the high level discrimination, the MICA-scale experiments are needed. MICA can detect the ice-soil borders and perform unique tomography of Antarctica.

PACS numbers: 14.60.Pq, 26.65.+t, 91.35.-x, 95.85.Ry, 96.60.Jw,

## I. INTRODUCTION

Oscillations of the solar neutrinos in the Earth [1] - [32] have the following features.

1. Due to loss of the propagation coherence, the solar neutrinos arrive at the surface of the Earth as independent fluxes of the mass eigenstates [8], [9, 15, 24].

2. Inside the Earth the mass states oscillate in multi-layer medium with smoothly (adiabatically) changing density within layers and sharp density change at the borders between the layers.

3. The oscillations proceed in the low density regime which is quantified by small parameter

$$\epsilon \equiv \frac{2VE}{\Delta m_{21}^2}, \quad (1)$$

where  $V(x) = \sqrt{2}G_F n_e(x)$  is the matter potential,  $n_e$  is the electron number density of the medium. For  $E = 10$  MeV at the surface of the Earth  $\epsilon$  equals  $\sim 0.03$ .

4. The oscillation length

$$l_m \approx l_\nu \approx 330 \text{ km} \left( \frac{E}{10 \text{ MeV}} \right) \left( \frac{7.5 \cdot 10^{-5} \text{ eV}^2}{\Delta m_{21}^2} \right)$$

is comparable to a section of trajectory in a layer  $d_i$  for trajectories with nadir angles  $\eta$  close to  $\pi/2$ :  $d_i = r_i / \cos \eta$ , where  $r_i \sim 10$  km is the width of the layer in the radial direction. The highest sensitivity is to structures of the density profile of the size  $\sim l_m/2$ .

5. The attenuation effect is realized in the order  $\epsilon$  due to the finite neutrino energy resolution (reconstruction) in the experimental setup [26, 32]. It means loss of sensitivity to remote structures of the Earth density profile. Consequently, only structures sufficiently close to a detector, and therefore to the surface of the Earth (crust, upper mantle), are mostly relevant for observations. This means that with the boron neutrinos, deep structures, like the core of the Earth, are not seen at the  $\epsilon$  level. The attenuation effect is absent in the order  $\epsilon^2$ . Thus, the solar neutrino tomography is essentially sensitive to the small scale structures in the crust and mantle of the Earth.

In previous computations, (see, e.g., [24], [20]) the density profile of the one-dimensional PREM model [33] was used. In this model, borders between layers have forms of ideal spheres. Recently several new three dimensional Earth models have been developed. They show several new features of the density profiles which have not been taken into account previously: (i) the borders between layers are not spherically symmetric but have irregular deviations from spheres; (ii) the profiles depend on the azimuthal angle; (iii) The profiles are non-symmetric with respect to the center of neutrino trajectory. The horizontal sizes of these structures are comparable to oscillation length which means that effectively they can smooth borders between layers as well as produce some new parametric effects in oscillations.

In the present paper, we study how these new features modify the observational effects. We compute the Earth

matter effect using new models. This allows us to assess a possibility do distinguish the models with solar neutrino detectors. At the same time, our computations quantify errors of the computed effects due to uncertainty in the density profile.

Presently there are first (about  $3\sigma$ ) indication of the Earth matter effect by SuperKamiokande [29], and this situation will stay till the next generation of experiments will start to operate. Here we consider solar neutrino studies by future detectors DUNE [34], Hyper-Kamiokande (HK)[35], THEIA [36] [37] and MICA [38].

The paper is organized as follows. In Sec. II, we present oscillation formalism relevant for our computations and elaborate on some new features, such as high order  $\epsilon$  corrections, entanglement, *etc.* We introduce the generalized energy resolution functions and study their properties. The Day-Night asymmetry is presented in terms of these resolution function and potential. In Sec. III, new models of the density distribution in the Earth are described. In Sec. IV, we present results of computations of the Earth matter effect for future detectors. Conclusions are given in Sec. V.

## II. RELATIVE EXCESS OF THE NIGHT EVENTS AND ATTENUATION

### Coherence and entanglement

Loss of the propagation coherence is due to spatial separation of the wave packets that correspond to the mass eigenstates originated from the same flavor state. Although separated, these wave packets belong to the same wave function and therefore entangled. If one of the eigenstates is detected the parts of the wave function, which describe two other eigenstates, collapse. It can be easily shown that observational result is the same as in the case of independent fluxes of mass eigenstates once total flux of these states is normalized on the total flux of the originally produced flavor neutrinos. Coherence is not restored in a realistic detector.

### Corrections to probability

Recall that the  $\nu_e$  survival probability during a day, as function of the neutrino energy, equals

$$P_D(E) = \frac{1}{2}c_{13}^4 [1 + \cos 2\theta_{12} \cos 2\bar{\theta}_{12}^m(E)] + s_{13}^4, \quad (2)$$

where  $c_{13} \equiv \cos \theta_{13}$ ,  $s_{13} \equiv \sin \theta_{13}$ , and  $\cos 2\bar{\theta}_{12}^m$  is the mixing parameter averaged over the boron neutrino production region in the Sun [40]:

$$\cos 2\bar{\theta}_{12}^m \approx \frac{\cos 2\theta_{12} - c_{13}^2 \bar{\epsilon}_\odot}{\sqrt{(\cos 2\theta_{12} - c_{13}^2 \bar{\epsilon}_\odot)^2 + \sin^2 2\theta_{12}}}. \quad (3)$$

Here

$$\bar{\epsilon}_\odot \equiv \frac{2\bar{V}_\odot E}{\Delta m_{21}^2} \quad (4)$$

and  $\bar{V}_\odot$  is the averaged matter potential in the  $^8\text{B}$  neutrino production region.

For high energy part of the boron neutrino spectrum, where  $\bar{\epsilon}_\odot \gg 1$ , we have

$$\cos 2\theta_{12}^m(E) \approx - \left[ 1 - \frac{\sin^2 2\theta_{12}}{2c_{13}^4} \left( \frac{\Delta m_{21}^2}{2\bar{V}_\odot E} \right) \right]. \quad (5)$$

So, dependence on  $E$  is weak. At the solar neutrino energies the matter effect on the 1-3 mixing is negligible, therefore  $\bar{\theta}_{13} \approx \theta_{13} = 8.4^\circ$  [39].

During a night the probability equals  $P_N = P_D + \Delta P$ , where the difference of the night and day probabilities is given to the order  $\epsilon^2$  by [26, 41]

$$\Delta P(E) = \kappa(E) \left[ \int_0^L dx V(x) \sin \phi^m(L-x, E) + I_2 \right]. \quad (6)$$

Here

$$\kappa(E) \equiv -\frac{1}{2}c_{13}^6 \cos 2\bar{\theta}_{12}^\odot(E) \sin^2 2\theta_{12} \approx 0.5$$

is slowly changing function of  $E$ , and

$$I_2 \equiv \frac{1}{2} \cos 2\theta_{12} \left[ \int_0^L dx V(x) \cos \phi^m(L-x) \right]^2 \quad (7)$$

is a correction of the order  $\epsilon^2$ , since in (7) each integral over  $x$  is of the order  $\epsilon$ . The integration in (7) proceeds along a neutrino trajectory. In new models of the Earth apart from the nadir angle  $\eta$  the density and potential profiles depend, also on position of the detector  $\mathbf{x}_D$  and azimuthal angle  $\phi_a$ :  $V = V(x, \mathbf{x}_D, \eta, \phi_a)$ . Correspondingly, for a given detector and a given of moment of time  $\Delta P = \Delta P(\mathbf{x}_D, \eta, \phi_a)$ .

In Eq. (6)

$$\phi^m(L-x, E) \equiv \int_x^L dx \Delta_{21}^m(x). \quad (8)$$

is the adiabatic phase acquired from a given point of trajectory  $x$  to a detector at  $L$ .  $\Delta_{21}^m(x)$  is the level splitting and in our calculations we use it up to the first order in  $\epsilon$ :

$$\begin{aligned} \Delta_{21}^m &= \Delta_{21} \sqrt{(\cos 2\theta_{21} - c_{13}^2 \epsilon)^2 + \sin^2 2\theta_{21}} \\ &\approx \Delta_{21} (1 - c_{13}^2 \cos 2\theta_{12} \epsilon). \end{aligned}$$

Here  $\Delta_{21} \equiv \Delta m_{21}^2 / 2E$  is the splitting in vacuum. Consequently, the oscillation phase (8) equals

$$\phi^m(L-x, E) = \Delta_{21} \left[ (L-x) - c_{13}^2 \cos 2\theta_{12} \int_x^L dx \epsilon(x) \right]. \quad (9)$$

Introducing the average density along a neutrino trajectory  $\bar{\rho}(\eta)$ , we can rewrite Eq. (9) as

$$\phi^m(L-x, E) = \phi_0^m + \delta\phi^m \quad (10)$$

where  $\phi_0^m \equiv \Delta_{21}(L-x)$  is the zero order phase and

$$\delta\phi^m = \phi_0^m c_{13}^2 \cos 2\theta_{12} \epsilon(\bar{\rho}), \quad (11)$$

is the phase shift due to the  $\epsilon$ -correction.

For  $\Delta m^2 = 7.5 \times 10^{-5} \text{ eV}^2$  and  $\rho = 5 \text{ g/cm}^3$  the relative size of the correction (second term in Eq. (10)) is about 3%. For large  $\phi_0^m$  the phase shift  $\delta\phi^m$  can be observable. E.g., if  $\phi_0^m = 5\pi$ , we find  $\delta\phi^m = 27^\circ$ .

The correction  $\delta\phi^m$  leads to the shift of oscillatory pattern in the  $\eta$  scale. Since  $\delta\phi^m = \Delta_{21}\delta L(\eta)$  and  $L = 2R \cos \eta$  we obtain

$$\delta\eta = \frac{\delta\phi^m}{2R \sin \eta \Delta_{21}}. \quad (12)$$

Insertion of expression for  $\delta\phi^m$  (11) in to (12) gives

$$\delta\eta = \cot \eta c_{13}^2 \cos 2\theta_{12} \epsilon. \quad (13)$$

For  $\eta = 70^\circ$  we obtain  $\delta\eta = 0.2^\circ$ , while period of oscillatory dependence in the  $\eta$  scale for this  $\eta$  equals  $2.8^\circ$ , *i.e.*, the shift is by 1/14 of the period.  $\delta\eta$  increases with decrease of  $\eta$ .

Let us consider  $I_2$  – the second term in (6). For constant density it can be computed explicitly

$$I_2 \approx 0.5 \cos 2\theta_{12} \bar{\epsilon}^2 \sin^2(L\Delta_{21}). \quad (14)$$

Apart from  $\bar{\epsilon}^2$ , this term contains additional small factor  $0.5 \cos 2\theta_{12} \approx 1/6$ . As a result,  $I_2$  is about 0.015% and therefore can be neglected. Our computational relative errors are of the order of 0.1%. Thus, the largest correction to the probability follows from  $\phi^m$ .

### Comments on adiabaticity

In the lowest order in  $\epsilon$ , the sensitivity to structures of the Earth matter profile, its deviation from constant density, appears due to borders between layers which strongly (maximally) break adiabaticity. Indeed, in the adiabatic case the oscillation probability would depend on density at the surface of the Earth and on the oscillation phase. However, in the lowest (zero) order in  $\epsilon$  the phase coincides with the vacuum phase. The matter correction to the phase is proportional to  $\epsilon$  which then appears as  $\epsilon^2$  in the probability. So, in the adiabatic case there is no sensitivity to the profile in the  $\epsilon$  order.

In general, deviations of borders between layers from spherical form may produce effective smearing of borders for neutrino trajectories with large  $\eta$ , and consequently, to decrease of the adiabaticity violation. That would lead to partial loss of sensitivity to the density profile.

If deviation from spherical form in radial direction,  $\Delta h$ , and in horizontal direction,  $l_f$ , are such that neutrino trajectory at certain  $\eta$  crosses the border between the same layers several (many) times, the density gradient along the trajectory will decrease. For density jump in a border  $\Delta\rho$  the gradient equals  $\Delta\rho \cos \eta / \Delta h$ . The scale of density change

$$l_\rho \equiv \rho(d\rho/dl)^{-1} = \frac{\rho}{\cos \eta \Delta\rho} \Delta h$$

should be compared with the oscillation length in the adiabaticity condition.

As we will see, typical scale of deviation of, e.g., the border between the crust and mantle from spherical form is  $\Delta h \sim 5-10 \text{ km}$  and the horizontal size of the structures is  $l_f \sim (70-150) \text{ km}$ . This gives the slope of the structure  $\eta_f \sim \Delta h/l_f \sim (2-7)^\circ$ . Therefore double crossing can occur for the trajectories with  $\eta > 83^\circ$ . For parameters of new Earth models, however, adiabaticity is still strongly broken and multiple crossing of borders can occur only in very narrow intervals of  $\eta$ .

In the lowest  $\epsilon$  order, the result for  $\Delta P(E)$  in (6) can be reproduced as a result of interference of the “oscillation waves” emitted from borders between layers [41]. For  $i$ th wave, the phase is determined by distance from border to a detector  $L-x_i$  and vacuum oscillation length, while the amplitude is proportional by the density jump  $\Delta\rho_i$  in the border. Then  $\Delta P(E)$  is the sum of the waves over borders which neutrino trajectory crosses. This representation gives simple interpretation of results of numerical computations.

### Attenuation and generalized energy resolution functions

The Earth matter effect can be quantified by the Day-Night asymmetry or the relative excess of night events (events rate) in energy range  $\Delta E$  as function of the nadir angle  $\eta$ :

$$A_{ND}(\eta, \Delta E) \equiv \frac{\Delta N_N(\eta, \Delta E)}{N_D(\Delta E)}, \quad \Delta N_N \equiv N_N - N_D. \quad (15)$$

Here  $N_N(\eta)$  and  $N_D$  are the numbers of night and day events (rates) correspondingly. The nadir  $\eta$  and azimuthal  $\phi_a$  angles are fixed by the detection time of an event. According to new models  $N_N(\eta)$  depends also on the position of a detector.

In experiments, the observables are the electron energy and direction. Therefore,  $\Delta E$  is determined by the observed energy interval of the produced (or recoil) electrons. In practice, we will use the energy of electrons above certain threshold. Thus, information on the density profile is encoded in the nadir angle dependence of the night excess. We will not consider the direction of electron.

Sensitivity of oscillations to the Earth density profile is determined by the sensitivity of a given experimental set-up to the true energy of neutrino  $E$ . This can be described by the generalized energy resolution function  $G_\nu(E^r, E)$  such that

$$\Delta N(E^r) = D \int dE G_\nu(E^r, E) \Delta P(E), \quad (16)$$

where  $E^r$  is the observed (reconstructed) neutrino energy or certain energy characteristic which can be measured in experiment. In (16)  $D$  is the factor which includes characteristics of detection: fiducial volume, exposure time, *etc.* It cancels in the expression for the relative excess  $A_{ND}$ . The resolution function is normalized as  $\int G_\nu(E^r, E) dE = 1$ . Similarly, one can write expression for  $N_D$ .

$G_\nu(E^r, E)$  includes the neutrino energy resolution function:  $g_\nu(E^r, E)$ , the energy dependence of the neutrino flux  $f_B(E)$  [40] and cross-section  $\sigma(E)$ :

$$G_\nu(E^r, E) \propto g_\nu(E^r, E) \sigma(E) f_B(E). \quad (17)$$

It should also include the energy dependent efficiency of detection.

Integration over the neutrino energy with the resolution function in Eq. (16) leads to the attenuation effect [24, 32]. Plugging expression for  $\Delta P(E)$  from (6) into (16) and neglecting  $I_2$  we obtain for  $\Delta N$

$$D \int_0^L dx V(x) \int_0^{E^{max}} dE G_\nu(E^r, E) \sin \phi^m(L-x, E). \quad (18)$$

Here integrations over  $x$  and  $E$  are interchanged. In this form the dependence of difference of events on structures of density profile is immediate.

Let us introduce the attenuation factor  $F(L-x)$  [24] such that the integral over  $E$  in Eq. (18) equals

$$\begin{aligned} & \int dE G_\nu(E^r, E) \sin \phi^m(L-x, E) \\ &= F(L-x) \sin \phi^m(L-x, E^r). \end{aligned} \quad (19)$$

In general, this equality can not be satisfied, but it is valid for special cases and under integral over  $x$ . Then the expression for  $\Delta N$  in (18) becomes

$$\Delta N(E^r) = D \int dx V(x) F(L-x) \sin \phi^m(L-x, E^r). \quad (20)$$

For the Gaussian form of  $G_\nu(E^r, E)$ , the attenuation factor is given by

$$F(d) \simeq e^{-2\left(\frac{d}{\lambda_{att}}\right)^2}, \quad (21)$$

where

$$\lambda_{att} \equiv l_\nu \frac{E}{\pi \sigma_E} \quad (22)$$

is the *attenuation length*, and  $l_\nu$  is the oscillation length in vacuum

$$l_\nu = \frac{4\pi E}{\Delta m_{21}^2}. \quad (23)$$

According to (20) and (21) for  $d \gg \lambda_{att}$  the attenuation factor  $F(d) \approx 0$ , and therefore contributions of remote structures to the integral (20) and therefore to observable oscillation effect is suppressed. For  $d = \lambda_{att}$  the factor  $F(d) = e^{-2} \approx 0.14$ , and the attenuation becomes significant. Consequently, the Day-night asymmetry depends mainly on the shallow structures of the Earth which are close to a detector.

For the ideal resolution,  $G_\nu(E^r, E) = \delta(E^r - E)$ , Eq. (19) gives  $F(L-x) = 1$ , which means that attenuation is absent.

The attenuation length is the distance at which oscillations integrated over the energy resolution interval  $\sigma_E$  are averaged out, or the difference of the oscillation phases for  $E$  and  $E + \sigma_E$  becomes larger than  $2\pi$  [32].

Expression (18) factorizes different dependences: The generalized resolution function encodes external characteristics: neutrino flux, cross-section, energy resolution of a detector.  $V(x)$  gives information about the density profile, oscillation probability is reduced to  $\sin \phi^m$ .

In what follows we will find expressions for the generalized reconstruction functions and present numbers of events in the form (18) separately for the  $\nu$ -nucleon and  $\nu - e$  scattering.

## Neutrino-nuclei scattering

We consider the charged current neutrino-nuclei interactions and the corresponding resolution function  $G_{\nu N}$ . If transitions to excited states are neglected, the energies of electron and neutrino are uniquely related (upto negligible nuclei recoil):  $E_e = E - \Delta E$ . Here  $\Delta E \approx \Delta M + m_e$  is the threshold of reaction. If transitions to excited states are significant but the energy of de-excitation is not measured, an additional uncertainty in reconstruction of the neutrino energy appears which should be included into  $G_{\nu N}$ .

The night-day difference of numbers of events with the observed energy of electron  $E_e^r$  is given by

$$\Delta N(E_e^r) = D \int_0^{E_e^{max}} dE_e g_e(E_e^r, E_e) \sigma(E) f_B(E) \Delta P(E), \quad (24)$$

where  $E = E_e + \Delta E$ ,  $E_e^{max}$  is maximal true energy of electron:  $E_e^{max} = E^{max} - \Delta E$ ,  $g_e(E_e^r, E_e)$  is the electron energy resolution function with  $E_e$  and  $E_e^r$  being the true and the observed energies correspondingly.

Introducing also  $E^r \equiv E_e^r + \Delta E$  and changing integration in (24) to integration over the neutrino energy  $E$  we

have

$$\Delta N(E_e^r) = D \int_{\Delta E}^{E^{max}} dE g_\nu(E^r, E) \sigma(E) f_B(E) \Delta P(E), \quad (25)$$

where  $g_\nu(E^r, E) \equiv g_e(E^r - \Delta E, E - \Delta E)$ . The equation (25) can be rewritten as

$$\Delta N(E_e^r) = Dz \sigma(E^r) f_B(E^r) \int_0^{E^{max}} dE G_{\nu N}(E^r, E) \Delta P(E), \quad (26)$$

with

$$G_{\nu N}(E^r, E) = z^{-1} g_\nu(E^r, E) \frac{\sigma(E) f_B(E)}{\sigma(E^r) f_B(E^r)}, \quad (27)$$

and  $z$  being the normalization factor. Inserting expression for  $\Delta P(E)$  from (6) into (26) and permuting integrations over  $x$  and  $E$  we obtain

$$\Delta N(E_e^r) = Dz \sigma(E^r) f_B(E^r) \kappa(E^r) \times \int dx V(x) \int_0^{E^{max}} dE G_{\nu N}(E^r, E) \sin \phi^m(x, E), \quad (28)$$

Integration over the energy can be removed introducing of the attenuation factor, as in (19), which gives

$$\Delta N(E_e^r) = Dz \sigma(E^r) f_B(E^r) \kappa(E^r) \times \int dx V(x) F_{\nu N}(L - x) \sin \phi^m(x, E^r). \quad (29)$$

Finally, integration over the interval of observed energies of electrons gives

$$\Delta N(\Delta E_e^r) = Dz \int_{E^{th}}^{E^{max}} dE^r \sigma(E^r) f_B(E^r) \kappa(E^r) \times \int dx V(x) F_{\nu N}(L - x) \sin \phi^m(x, E^r), \quad (30)$$

where we again substituted integration over  $E_e$  by integration over  $E$ .

For the day signal, which does not depend practically on  $\eta$ , we have

$$N_D(\Delta E_e^r) = Dz \int_{E^{min}}^{E^{max}} dE^r \sigma(E^r) f_B(E^r) P_D(E^r) \times \int_{\Delta E}^{E^{max}} dE G_{\nu N}(E^r, E). \quad (31)$$

Notice that if threshold  $\Delta E$  is low enough, the second integral over the resolution function is  $\approx 1$ , so that

$$N_D(\Delta E_e^r) = Dz \int_{E^{min}}^{E^{max}} dE^r \sigma(E^r) f_B(E^r) P_D(E^r). \quad (32)$$

The factors  $Dz$  cancel in the expression for  $A_{ND}$ .

Let us consider  $G_{\nu N}(E^r, E)$  defined in Eq. (27) in details. We take the Gaussian form for  $g_\nu(E^r, E)$  with

central energy  $E^c = E^r$  and  $\sigma_E = 0.1E^r$ . Fig. 1 (upper panel) shows dependence of  $G_{\nu N}$  on energy for several values of  $E^r$  computed with  $\sigma \propto Ep$ . We compare this dependence with Gaussian form  $G_{\nu N} = g^{Gauss}(E^r, E)$ . The flux of Boron neutrinos,  $f_B(E)$ , is taken from [40]. For convenience of comparison we normalized  $G_{\nu N}(E^r, E)$  (dashed lines) such that  $G_{\nu N}(E^r, E)^{max} = g^{Gauss}(E^r, E)^{max}$ , and the y-axis is in arbitrary unit.

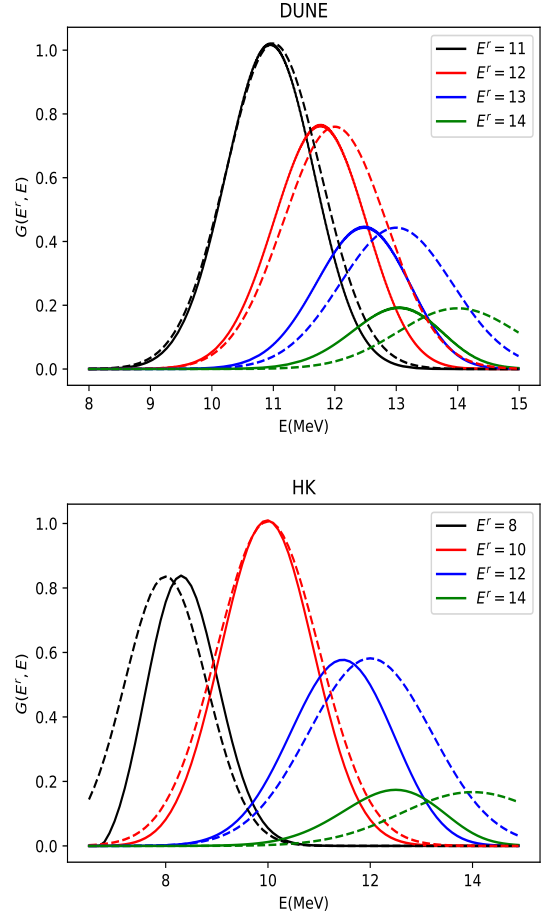


FIG. 1: Dependences of the neutrino energy resolution functions  $G_\nu(E^r, E) = g_\nu(E^r, E) \sigma(E) f_B(E)$  (solid lines) and  $G_\nu(E^r, E) = g^{Gauss}(E^r, E)$  (dashed lines) on true neutrino energy  $E$  for different values of the reconstructed neutrino energy  $E^r$ . For  $g_\nu(E^r, E)$  we take the Gaussian distribution with width  $\sigma_E = 0.1E^r$ . Upper panel:  $G_{\nu N}$  - for experiments based on the  $\nu e$ - nuclei scattering. Lower panel:  $G_{\nu e}$  - for experiments based on the  $\nu - e$  scattering with cut  $E_e > 6.5$  MeV.

The product  $\sigma(E) f_B(E)$  has the form of a wide asymmetric peak with maximum at  $\sim 11$  MeV. Consequently for  $E^r = 11$  MeV the generalized function  $G_{\nu N}$  is close to the corresponding Gaussian form with energy of maximum  $E^c \approx E^r$ , while for  $E^r > 11$  MeV the factor  $\sigma(E) f_B(E)$  shifts  $G_{\nu N}$  to lower energies  $E^c < E^r$  and

reduces the width: According to Fig. 1 for  $E^r = 12$  MeV the energy of maximum  $E^c = 11.7$  MeV and the relative width  $\sigma_E/E = 0.074$  instead of 0.1 in  $g_\nu$ . The change becomes more profound with increase of  $E^r$ . For  $E^r = 14$  MeV we find  $E^c = 13.1$  MeV and  $\sigma_E/E = 0.069$ . Thus, the energy dependence of  $\sigma f_B$  leads to better energy resolution and therefore to increase the attenuation length which means the improvement of sensitivity to remote structures.

According to Fig. 1, for Gaussian  $g_\nu$ , the whole effective resolution function  $G_{\nu N}$  can be well approximated by the Gaussian function with appropriately chosen energy of maximum,  $E^c = E^c(E^r) \neq E^r$ , and width  $\sigma_E = \sigma(E^r)$ . In fact, a priori the form of  $g_\nu(E^r, E)$  is not known and eventually will be determined in experiment. Therefore in our computations we will use the generalized reconstruction function in the Gaussian form:

$$G_{\nu N}(E^r, E) \approx g^{Gauss}[E, E^{max}(E^r), \sigma(E^r)]. \quad (33)$$

Under integration over the neutrino energy  $E$  the difference of results for  $A_{ND}$  computed with the Gaussian  $G_{\nu N}$  (33) and  $G_{\nu N}$  with Gaussian  $g_\nu$  is negligible. Using the PREM model we find that the relative difference results for  $A_{ND}$  is smaller than 0.3%.

### Neutrino-electron scattering

In this case the energies of neutrino and electron are not uniquely related, but correlated via the differential cross-section  $d\sigma(E, E_e)/dE_e$ . Correspondingly, expression for the effective resolution function in (18) will differ from  $G_{\nu N}$ . [49]

The difference of numbers of the night and day events with a given observed energy of electron  $E_e^r$  equals

$$\begin{aligned} \Delta N(E_e^r) &= D \int_0^{E^{max}} dE_e g_e(E_e^r, E_e) \\ &\times \int_{E_e}^{E^{max}} dE \frac{d\sigma_\Delta(E, E_e)}{dE_e} \Delta P(E) f_B(E), \end{aligned} \quad (34)$$

where

$$\frac{d\sigma_\Delta(E, E_e)}{dE_e} \equiv \frac{d\sigma_e(E, E_e)}{dE_e} - \frac{d\sigma_\mu(E, E_e)}{dE_e} \quad (35)$$

is the difference of the charged current,  $d\sigma_e/dE_e$ , and neutral current,  $d\sigma_\mu/dE_e$ , differential cross-sections. Interchanging integrations over  $E_e$  and  $E$  in Eq. (34) we obtain

$$\Delta N(E_e^r) = D \int_0^{E^{max}} dE \Delta P(E) f_B(E) \sigma_\Delta(E) g_\nu(E_e^r, E), \quad (36)$$

where

$$g_\nu(E_e^r, E) \equiv \frac{1}{\sigma_\Delta(E)} \int_0^E dE_e \frac{d\sigma_\Delta(E, E_e)}{dE_e} g_e(E_e^r, E_e), \quad (37)$$

and

$$\sigma_\Delta(E) = \int_0^E dE_e \frac{d\sigma_\Delta(E, E_e)}{dE_e}. \quad (38)$$

The generalized reconstruction function can be introduced similarly to (27):

$$G_{\nu e}(E_e^r, E) = z^{-1} g_\nu(E, E_e^r) \frac{f_B(E) \sigma_\Delta(E)}{f_B(E_e^r) \sigma_\Delta(E_e^r)}, \quad (39)$$

or explicitly, inserting  $g_\nu$  from (37), as

$$\begin{aligned} G_{\nu e}(E_e^r, E) &= \frac{z^{-1} f_B(E)}{f_B(E_e^r) \sigma_\Delta(E_e^r)} \\ &\times \int_0^E dE_e \frac{d\sigma_\Delta(E, E_e)}{dE_e} g_e(E_e, E_e^r). \end{aligned} \quad (40)$$

The only difference from (27) is that here in  $g_\nu$  the electron resolution function is integrated with the differential cross-section.

Instead of  $E_e^r$  we can introduce the ‘‘observable’’ neutrino energy  $E^r = E^r(E_e^r)$  defined as the energy of maximum of  $G_{\nu e}$  for a given  $E_e^r$ :

$$G_{\nu e}(E_e^r, E^r) = G_{\nu e}^{max}(E_e^r). \quad (41)$$

In terms of  $G_{\nu e}(E_e^r, E)$  the N-D difference of numbers of events can be presented as

$$\begin{aligned} \Delta N(E_e^r) &= Dz f_B(E^r(E_e^r)) \sigma_\Delta(E^r(E_e^r)) \times \\ &\int_0^{E^{max}} dE \Delta P(E) G_{\nu e}(E^r(E_e^r), E). \end{aligned} \quad (42)$$

As in the  $\nu N$ - case, we insert explicit expression for  $\Delta P(E)$  and interchange integration over  $x$  and  $E$ . Then the integration over  $E$  can be removed introducing the attenuation factor which gives

$$\begin{aligned} \Delta N(E_e^r) &= Dz f_B(E^r) \sigma_\Delta(E^r) \kappa(E^r) \times \\ &\int dx V(x) F_{\nu e}(L-x) \sin \phi^m(x, E^r), \end{aligned} \quad (43)$$

where  $F_{\nu e}(L-x)$  corresponds to  $G_{\nu e}(E^r, E)$ .

The difference of numbers of events with the observable energy of electrons in the interval  $\Delta E_e^r \equiv (E_e^{r, min} - E_e^{r, max})$  equals

$$\begin{aligned} \Delta N(\Delta E_e^r) &= Dz \int_{E_e^{r, min}}^{E_e^{r, max}} dE_e^r f_B(E^r) \sigma_\Delta(E^r) \kappa(E^r) \\ &\int dx V(x) F_{\nu e}(L-x) \sin \phi^m(x, E^r), \end{aligned} \quad (44)$$

and  $E^r = E^r(E_e^r)$  is determined by (41).

The number (rate) of events with the observed electron energy  $E_e^r$  during a day equals

$$\begin{aligned} N_D(E_e^r) &= \int_0^{E^{max}} dE f_B(E) [P_D(E) \sigma^e(E, E_e^{th}) g_\nu^e(E_e^r, E) \\ &+ (1 - P_D(E)) \sigma^\mu(E, E_e^{th}) g_\nu^\mu(E_e^r, E)]. \end{aligned} \quad (45)$$

Here

$$g_{\nu}^{e,\mu}(E_e^r, E) \equiv \int_0^E dE_e \frac{d\sigma_{e,\mu}(E, E_e)}{\sigma_e(E)dE_e} g_e(E_e^r, E_e). \quad (46)$$

The total cross-sections are given by

$$\sigma_{e,\mu}(E) = \int_0^E dE_e \frac{d\sigma_{e,\mu}(E, E_e)}{dE_e}.$$

Expression (45) can be simplified assuming  $g_{\nu}^{\mu} \approx g_{\nu}^e \approx g_{\nu}$ :

$$N_D(E_e^r) = \int_0^{E_e^{max}} dE f_B(E) g_{\nu}(E_e^r, E) [P_D(E) \sigma^e(E, E_e^{th}) + (1 - P_D(E)) \sigma^{\mu}(E, E_e^{th})]. \quad (47)$$

Let us consider  $G_{\nu e}(E, E_e^r)$  in detail. In the bottom panel of Fig. 1 we show  $G_{\nu e}(E, E_e^r)$  as function of  $E$  computed according to Eq. (40). For the  $\nu - e$  scattering the product  $\sigma(E) f_B(E)$  has wide peak with maximum at  $E = 10$  MeV, and additional weak  $E$  - dependence comes from the integral in (40). Therefore the smallest deviation of  $G_{\nu e}(E_e^r, E)$  from the Gaussian form is at  $E^r \sim 10$  MeV. For  $E^r < 10$  MeV the maximum of  $G_{\nu e}$  is shifted to higher energies, while  $E^r > 10$  MeV - to lower energies. In both cases the width of  $G_{\nu e}$  decreases. According to Fig. 1 (bottom) for  $E^r = 8$  MeV the maximum of  $G_{\nu e}$  is shifted with respect to  $E^r$  to higher energy by 0.3 MeV, and the width is slightly smaller. For  $E^r = 12$  MeV, inversely, the maximum is shifted to  $E^c = 11.7$  MeV, and the width becomes  $\sigma_E/E = 0.085$ . This trend (due to fast decrease of the flux with energy above 10 - 11 MeV) is even more significant for larger  $E^r$ : at  $E^r = 14$  MeV, we find  $E^c = 12.6$  MeV and  $\sigma_E/E = 0.08$ . Again, taking into account the energy dependence of  $\sigma$  and  $f_B$  improves the energy resolution, but weaker than in the  $\nu N$  case.

The biggest contribution to oscillation effect comes from the energy range (10 - 12) MeV, where  $G_{\nu e}$  is rather close to the Gaussian form. Therefore in computations we will use the Gaussian form for  $G_{\nu e}$ , and consequently, the attenuation factor in the form (21). Inclusion of the flux and cross-section energy dependences narrows the resolution function.

In expressions for  $\Delta N$  the  $\phi_a$  dependence appears in two places: in the potential:  $V = V(x, \eta, \phi_a)$  and in the phase  $\phi^m = \phi^m(\phi_a)$ . For each  $\eta$  and position of the detector we performed averaging of  $\Delta N$  over the azimuthal angle  $\phi_a$ . If  $\phi_a$  dependence of the phase is neglected, in the first approximation, the averaging of  $\Delta N$  over  $\phi_a$  is reduced to averaging of the potential.

### III. MODELS OF THE EARTH AND DENSITY PROFILES

In computations, we used density profiles reconstructed from recently developed 3D models of the Earth.

Due to the attenuation effect, the Day-Night asymmetry mainly depends on shallow density structures: crust, upper mantle and crust-mantle border called Moho, or Mohorovicic discontinuity. There are two types of crust: the oceanic crust and the continental one. The width of oceanic crust is about (5 - 10) km, while the continental crust is thicker: (20 - 90) km [46, 47]. The predicted depth of Moho,  $h_{Moho}$ , significantly varies for different models. In contrast, the density change in the Moho is nearly the same for all the models. Beneath Homestake the jump is from 2.9 gr/cm<sup>3</sup> to 3.3 gr/cm<sup>3</sup>.

A brief description of relevant elements of the models is given below.

1. The Shen-Ritzwoller model (S-R) [42] is based on joint Bayesian Monte Carlo inversion of geophysical data. It gives the density profile of the crust and uppermost mantle beneath the US, in area with latitudes (20° - 50°) and longitudes (235° - 295°). In the radial direction it provides the density change from the sea level surface down to the depth of 150 km with  $h_{Moho} = 52$  km beneath the Homestake (see Fig. 2).

2. FWEA18, the Full Waveform Inversion of East Asia model [43], covers the latitudes 10° - 60° and longitudes 90° - 150°. It gives the density profile from the surface down to 800 km, and  $h_{Moho} = 33$  km beneath Kamioka.

3. SAW642AN [44] is a global (all latitudes and longitudes) radially anisotropic mantle shear velocity model based on a global three-dimensional tomography of the Earth. The model gives the density profile of mantle starting from the depth of Moho,  $h_{Moho} = 24$  km, down to 2900 km. No crust structure is available.

4. CRUST1 [45] is a global 3D model, that presents data with 1×1 degree grid in latitude and longitude at the surface. It gives the density and depth of borders of eight layers of the crust: water, ice, upper sediments, middle sediments, lower sediments, upper crust, middle crust, lower crust. The model predicts the depths of Moho  $h_{Moho} = 48$  km and  $h_{Moho} = 40$  km beneath Homestake and Kamioka respectively and nearly constant density of the upper mantle down to 100 km. It provides also the density distribution above the sea level.

Using these models we reconstructed the density, and consequently  $V(x)$ , profiles along neutrino trajectories determined by position of detectors,  $\eta$  and  $\phi_a$ . Maximal depths  $h^{max}$  down to which the models provide data are  $h^{max}(S - R) = 150$  km,  $h^{max}(CRUST1) \approx 80$  km,  $h^{max}(FWEA18) = 800$  km,  $h^{max}(SAW642AN) = 2900$  km. Therefore we reconstructed the density profiles using the following prescription:

- for the S-R, CRUST1 and FWEA18 models with relatively small  $h^{max}$  we take the SAW642AN profile in the range  $h = h^{max} - 2900$  km.
- Below 2900 km for all the models we use the PREM profile. Recall that PREM - the Preliminary reference Earth model is a one-dimensional model that

represents the average (over solid angle) density of the Earth as a function of depth. The depth of Moho in the PREM model equals  $h_{Moho} = 24.4$  km.

Due to attenuation effect possible uncertainties related to these compilations of the profiles do not change results significantly even for small nadir angles.

- For purely mantle model SAW642AN above Moho,  $h = (0 - 24)$  km, we take constant density  $\rho = \rho_{SAW}(24 \text{ km})$ .

All the models, but CRUST1, give the density below the sea level. In all simulations, except the case of MICA, we consider the surface of Earth as perfect sphere and take zero density above the sea level. Effect of these simplifications is much smaller than sensitivity of all experiments (but MICA) due to restricted statistics. In the case of MICA, we have taken into account the Earth structures above sea level.

In Fig. 2, we present the S-R and CRUST1 density profiles beneath Homestake for fixed latitude  $44.35^\circ$ . Both models provide data for this place down to 80 km. Shown is the depth of layers with a given density as function of longitude (azimuthal angle). Notice that at the latitude  $44^\circ$  the  $1^\circ$  of longitude corresponds to 76 km at the surface. The black curves show Moho depth, where density jumps approximately from 2.9 to 3.3 g/cm<sup>3</sup>.

Few comments are in order.

1. The surfaces of equal density, and in particular, borders between layers deviate from spherical form.
2. There are irregular deviations from spherical form with typical angular size  $(2 - 5)^\circ$  or  $(150 - 400)$  km, which is comparable with the oscillation length. The depth variation,  $\delta h$ , is up to  $(5 - 10)$  km, *i.e.* up to 30%.
3. There are narrow spikes of large amplitude and wide regions  $\sim 10^\circ$ , where the depth increases by 30% with respect to average value.
4. Two models give rather similar density distributions: the average depths and lengths are similar. At the same time, variations of S-R and CRUST1 models are not correlated.

In the case of spherical inner structures the nadir angle  $\eta_c$  at which neutrino starts to cross a given border between layers with the depth  $h$  equals

$$\sin \eta_c = 1 - \frac{h}{r_E}, \quad (48)$$

where  $r_E = 6371$  km is the radius of the Earth. For  $\eta < \eta_c$  neutrino crosses this border twice. Neutrino “sees” the mantle for the first time at  $\eta_{Moho} = 83.6^\circ$  in the S-R model, at  $\eta_{Moho} = 83.4^\circ$  in the CRUST1 model and at  $\eta_{Moho} = 84.9^\circ$  in the SAW642AN model on September 23 (where the date fixes the azimuthal angle).

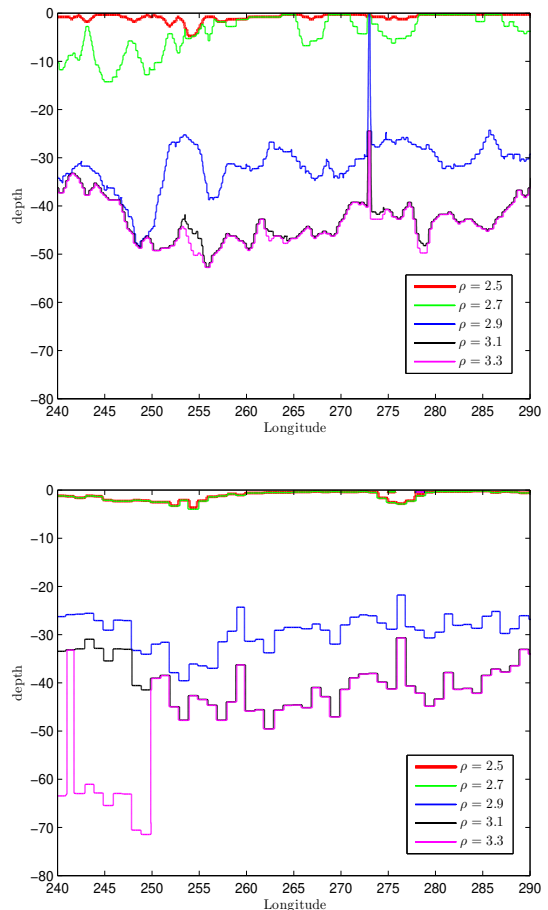


FIG. 2: Depth of layers with several fixed densities beneath the Homestake mine (the latitude  $44.35^\circ$ ) as function of the azimuthal angle (longitude). Upper plot: Shen-Ritzwoller model, bottom plot: the CRUST1 model. The black lines show the depth of Moho.

The noticeable difference between the S-R (CRUST1) profile and SAW642AN profile appears above the S-R Moho depth  $h > 52$  km. Below S-R Moho all three models give similar results.

According to Fig. 2 there are deviations of Moho from of ideal sphere of two types:

- 1) Relatively small variations of  $2 - 5^\circ$  scale which would correspond to  $(150 - 400)$  km at the DUNE latitude and the size (depth)  $\pm(2 - 5)$  km.
- 2) Long (continental) scale variations of size  $50^\circ$  with depth 20 km such that the smallest depth,  $h_{min} = 32$  km, is close to ocean and the bigger depth  $h_{max} = 52$  km is in the center of continent. This means that the Moho border varies within the shell (we call it Moho shell) restricted by spherical surfaces with depth 32 – 52 km and average depth 42 km.

The length of neutrino trajectory within the Moho shell equals  $\approx 2\sqrt{2}r_E(h_{max} - h_{min}) \approx 710$  km which



is 2 times bigger than the oscillation length. According to (48) borders of the Moho shell are seen from a detector site at  $\eta_{min} = 84.2^\circ$  and  $\eta_{max} = 82.7^\circ$ . So that for  $\eta > \eta_{min}$  there is no crossings of Moho: in the interval  $\eta = (\eta_{min} - \eta_{max})$  one may expect multiple crossing of Moho and since horizontal scale of variations of the border is comparable to the oscillation length, parametric effects are expected. However, averaging over azimuthal angle washes out these effects. For  $\eta < \eta_{max}$  neutrino trajectory crosses the Moho shell twice, and within each crossing it can be more than one crossing of the Moho border. Substantial effect due to Moho crossings is expected at  $\eta \sim 83^\circ$ .

Below  $83^\circ$  neutrinos cross the Moho in all the models. For smaller  $\eta$  the differences in these models become small.

As an example, in Fig. 3, we show the reconstructed density profiles of three models along the neutrino trajectory which ends at Homestake with  $\eta = 75^\circ$  on September 23. The length of trajectory equals 3295 km. According to Fig. 3 neutrinos cross the Moho border second time after 3055 km at a depth of 46 km in the S-R model. For CRUST1 model the corresponding numbers are 3121 km and 43 km, while for SAW642AN model they equal 3198 km and 24 km.

In Fig. 4, similar profiles are shown at the Hida place and or nadir angle  $75^\circ$ .

Clearly the profiles are not symmetric. Moreover, the density decreases to the middle of trajectory, especially for Homestake. This is related to thicker crust in the middle of a continent.

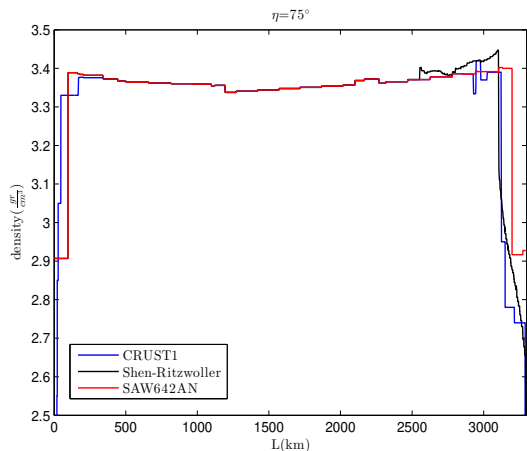


FIG. 3: The density of the Earth along the neutrino trajectory at nadir angle  $75^\circ$ , and detector in Homestake mine as a function of distance from the point of entering the Earth.

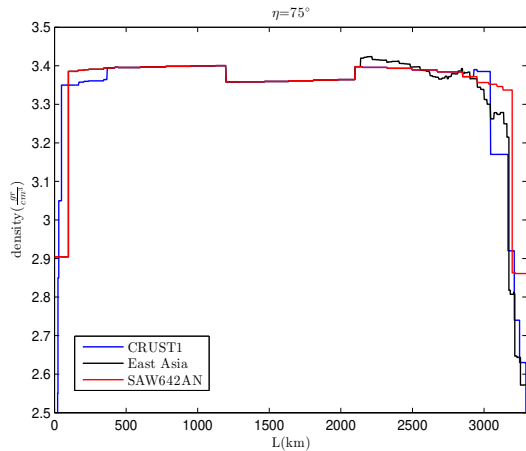


FIG. 4: The same as in Fig. 3 but for the detector located at Hida.

#### IV. PREDICTIONS FOR FUTURE EXPERIMENTS

We compute the oscillation probability during a day time,  $P_D(E)$ , according to Eq. (2). The rate of events is found using Eq. (31) for  $\nu N$ - scattering and Eq. (47) for the  $\nu e$ - scattering. The excess of night event rate was computed using expression in (32) for the  $\nu N$ - scattering and the one in (44) for the  $\nu e$ - scattering. These expressions correspond to  $\Delta P$  with neglected  $I_2$ , while the phase was computed keeping the  $\epsilon$  correction.

We take the generalized resolution functions  $G_{\nu N}(E^r, E)$  and  $G_{\nu e}(E^r, E)$  in the Gaussian form with certain values of the relative widths,  $\sigma_E/E$ . The nadir angle and  $A_{ND}(\eta, \phi_a)$  are computed with one minute time intervals during a year. Then we averaged  $A_{ND}(\eta, \phi_a)$  over the azimuthal angle  $\phi_a$ .

To check the stability of the results with respect to the time binning, we calculated  $A_{ND}(\eta)$  for several values of  $\eta$  with time intervals 15 seconds. Since the starting time of calculation is arbitrary,  $A_{ND}$  was also computed with 30 seconds shift. We find that the results are stable with respect to these variations and their relative changes are less than 0.1%.

We compute numerically the annual exposures for detectors at Homestake, Hida, and MICA as functions of nadir angle with  $\Delta\eta = 0.1^\circ$  (see Fig. 5). The exposure functions for Homestake is in agreement with that in Ref. [41]. The asymmetry averaged over the year is given by integration of  $A_{DN}$  with the exposure (weight) function  $W(\eta)$  over  $\eta$ :

$$\bar{A}_{DN} = \int d\eta W(\eta) A_{DN}(\eta).$$

We used exposure functions to compute the expected experimental errors for different  $\eta$ -intervals. The value

$\Delta m_{21}^2 = 7.5 \times 10^{-5} \text{ eV}^2$  is used unless specially indicated.

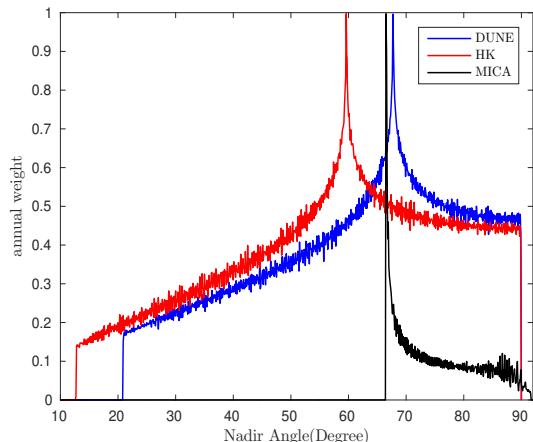
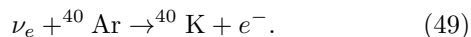


FIG. 5: Annual exposure of the detector as a function of nadir angle for the detectors at Homestake mine, Hida Kamioka and South pole with the time resolution of one minute and nadir angle resolution of  $0.1^\circ$ .

## DUNE

DUNE is the 40 kt liquid argon TPC which may detect solar neutrinos via the charged current process



For this process we use a generic form of cross-section

$$\sigma_{CC}(E) = A p_e E_e, \quad (50)$$

where  $A$  is a factor irrelevant for the relative excess,  $p_e$  is the momentum and  $E_e = E_\nu - \Delta M$  is the energy of electron with  $\Delta M = 5.8 \text{ MeV}$  being the reaction threshold [41]. Only 9.7% of  ${}^8\text{B}$  neutrinos have energy  $E_\nu > 11 \text{ MeV}$  but due to strong energy dependence in (50) the corresponding fraction of detected events is 0.9. Therefore, we use the threshold 11 MeV to achieve higher energy reconstruction. For  $g_e$  we use the width  $\sigma_E/E = 0.1$ . With this arrangement  $\sigma_E/E = 7\%$ , and consequently, the attenuation length equals  $\lambda_{att} = 1800 \text{ km}$  for the average energy 12 MeV. The nadir angle at which the length of trajectory  $L > \lambda_{att}$  is  $\eta_{att} = 82^\circ$ . For  $\eta < \eta_{att}$  the Earth structures on the remote part of a neutrino trajectory become invisible.

Results of computations of  $A_{ND}(\eta)$  with the S-R, CRUST1 and SAW642AN density profiles are presented in Fig. 6.

Generic features of the  $\eta$  dependence of  $A_{ND}$  are the following:

(i) Oscillations in crust: Regular oscillatory pattern for  $\eta > \eta_{Moho}$ , *i.e.*  $\eta \sim 85^\circ - 90^\circ$  with decreasing depth due

to averaging. The third oscillatory peak can be affected by small density jumps in the crust. This quasi-regular oscillatory pattern is broken at  $\eta_{Moho}$ .

(ii) Moho interference: At  $\eta < \eta_{Moho}$  neutrino trajectory crosses the Moho border twice leading to interference of oscillation waves from two crossings. For some models and values of  $\Delta m_{21}^2$  the destructive interference of the waves leads to a dip at  $\eta_{dip}$  (for DUNE) which depends on  $\eta_{Moho}$ . This can also be interpreted as a parametric suppression of oscillations [41].

(iii) Rise of asymmetry: For  $\eta < \eta_{dip}$ , the asymmetry  $A_{ND}$  increases with decrease of  $\eta$ . The increase is due to the fact that for small  $\eta$  the section of the neutrino trajectory in the crust becomes much smaller than the oscillation length, and so the effective initial and final densities (averaged over the oscillation length) become larger, being determined by the mantle density.

(iv). In the region  $\eta < \eta_{dip}$  there are bump and another dip due to effect of density jumps in the mantle at the depths 400 and 670 km.

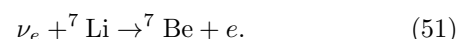
(v) The core of the Earth  $\eta_{core} = 33^\circ$  is not seen practically, producing  $\sim \epsilon^2$  effect at  $\eta < \eta_{core}$ .

We find that about 27000  $\nu_e$  events (49) can be detected annually with  $E_\nu > 11 \text{ MeV}$  in the 40 kt fiducial volume according to the CRUST1 model. The crosses show the expected errors  $A_{ND}(\eta)$  after twenty years of data taking. Statistical errors (computed using the exposure function) are taken into account only and no background was considered. As follows from Fig. 6, the largest difference between SAW642AN and S-R models as well as SAW642AN and CRUST1, is in the interval  $\eta = 60^\circ - 75^\circ$  and it originates mainly from different depths of Moho. The difference equals  $\Delta A_{ND}(\eta) \sim 0.006$  (15%) which is slightly above  $1\sigma$  C.L., after 20 years of data taking. The difference between CRUST1 and S-R models is practically negligible. Averaging of  $A_{ND}(\eta)$  over  $\eta$  leads to  $\bar{A}_{ND} = 0.040, 0.040$  and  $0.043$ , for CRUST1, S-R, and SAW642AN models, respectively, and precision of measurement of  $\bar{A}_{ND}$  will be 0.002.

The dependence of  $A_{ND}$  on  $\eta$  in DUNE experiment computed with SAW642AN model (red line Fig. 6) is similar to that in [41] for the PREM model. It has a dip at  $\eta_{dip} = 82^\circ$  and then increase of  $A_{ND}$  with decrease of  $\eta$ . Another dip appears at  $\eta = 44^\circ$ . In our present computations (SAW642AN) the dependence  $A_{ND}(\eta)$  is smoother than in [41] below the dip.

## THEIA

THEIA is a proposed 30 kT water-based liquid scintillator detector loaded with 1%  ${}^7\text{Li}$  [37]. It will be placed in Homestake. Neutrinos can be detected by the charged-current process



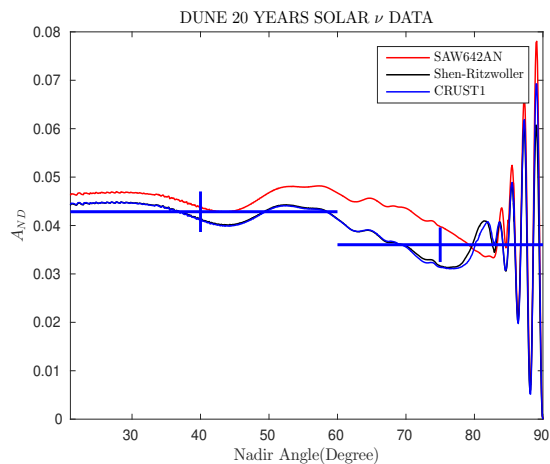


FIG. 6: The Night-Day asymmetry at DUNE as a function of nadir angle for SAW642AN, Shen-Ritzwoller, and CRUST1 models. The crosses present the expected accuracy of measurements after twenty years of exposure for the CRUST1 model.

The cross-section of this process is known with high precision [36] [37]. About 5000 events are expected annually with  $E_\nu > 5$  MeV. For THEIA we assume  $\sigma_E/E = 12\%$ . Therefore much lower statistics and worse energy resolution make THEIA in the present configuration less suitable for tomography than DUNE.

Since THEIA and DUNE are in the same place the results for  $A_{ND}(\eta)$  are similar (see Fig. 7). The difference between  $A_{ND}$  in THEIA and DUNE is due to lower energy threshold in THEIA, which means that effective neutrino energy, and consequently, the oscillation as well as the attenuation lengths are smaller. This, in turn, leads to different interference effects and lower sensitivity to remote structures in THEIA. The difference disappears when the same energy thresholds are taken.

For THEIA maximal difference of  $A_{ND}(\eta)$  computed with S-R and SAW642AN models (and also between CRUST1 and SAW642AN) is about  $A_{ND} = 0.005$ , which is smaller than  $1\sigma$  precision after 20 years of exposure. The difference between S-R and CRUST1 profile results is much smaller. The values of  $A_{ND}$  averaged over  $\eta$  with exposure taken into account equal to 0.024 (CRUST1), 0.024 (S-R) and 0.027 (SAW642AN).

The discrimination between the S-R and CRUST1 models can be improved if for each nadir angle  $\eta$  the range of azimuthal angle  $\phi_a$  is divided into two parts: in the first part  $\bar{\rho}_{SR} > \bar{\rho}_{CRUST1}$ , and in the second one  $\bar{\rho}_{SR} < \bar{\rho}_{CRUST1}$ . Then calculating  $A_{ND}$  in each of these parts separately and summing up moduli of differences one can avoid averaging.

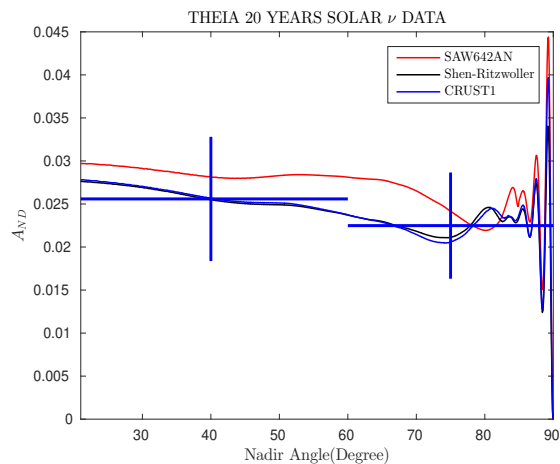


FIG. 7: The same as in Fig. 6, but for THEIA.

### Hyper-Kamiokande

Hyper-Kamiokande (HK) will detect the solar neutrinos by the  $\nu - e$  elastic scattering with 6.5 MeV threshold [35]. We take  $\sigma_E/E = 15\%$  as a tentative value. This gives the attenuation length  $\lambda_{att} = 700$  km for  $E = 10$  MeV.

In Fig. 8, we show the excess of night events computed with FWEA18, SAW642AN and CRUST1 density profiles. For  $d_{Moho} = 33$  km (FWEA18) the nadir angle  $\eta_{Moho} = 84.15^\circ$ , and the length of the trajectory  $L = 1300$  km, so, remote half of this trajectory will not contribute to the oscillation effect. The dip appears at  $\eta_{dip} = 78^\circ$  which is intermediate between CRUST1 and SAW64AN.

According to Fig. 8 maximal difference of  $A_{ND}$  in HK computed with FWEA18 and SAW642AN:  $\Delta A_{ND} = 0.003$ , appears in the wide range of nadir angles:  $\eta = 10^\circ - 80^\circ$ . The difference is more than  $1\sigma$  C.L. after 20 year of exposure with fiducial volume 0.56 Mton. For SAW642AN model the  $\eta$  dependence in HK is similar to that in THEIA detector. CRUST1 and FWEA18 have the biggest difference  $\Delta A_{ND} = 0.004$  in narrow range  $\eta = 75^\circ - 80^\circ$ . Notice that CRUST1 does not produce the dip which is a model dependent feature. The difference between CRUST1 and FWEA18 as well as SAW642AN is  $1\sigma$  C.L. The expected averaged asymmetry  $A_{ND}$  in HK equals 0.020 (FWEA18), 0.022 (CRUST1) and 0.024 (SAW642AN). Precision of measurements of  $A_{ND}$  will be 0.002.

The absolute value of asymmetry is substantially smaller than that for DUNE for two reasons: damping due to contribution from NC scattering, which is 0.76, and difference of averaged energies  $E_{HK}/E_{DUNE} = 0.75$ .

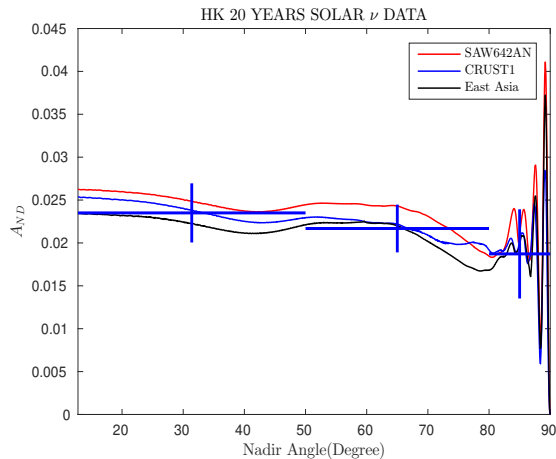


FIG. 8: The Day-night asymmetry at Hyper-Kamiokande as function of the nadir angle for CRUST1, FWEA18 and SAW642AN profiles. The crosses present expected accuracy of measurements after twenty years of exposure taking CRUST1 as the true model.

### MICA

The Megaton scale Ice Cherenkov Array (MICA) is a proposed detector at Amundsen-Scott South Pole station [38] in the same place as ICECUBE. The latitude and longitude of MICA are  $89.99^\circ$  south and  $63.45^\circ$  west correspondingly. Crustal structures under Antarctica are not well known due to a lack of seismic data [48], and therefore it is interesting to explore potential of a solar neutrino detector to determine this structure.

The detection is based on the  $\nu - e$  elastic scattering. In our calculations we took the characteristics of MICA from Ref. [38]: 10 Mton fiducial mass and 10 MeV energy threshold for the kinetic energy of the recoil electron. With these parameters, we find that about  $5 \times 10^5$  solar  $\nu e$ - scattering events are expected per year. For the energy resolution we use  $\sigma_E/E = 15\%$ . We consider the MICA detector at a depth of 2.25 km below the icecap (as the Deep Core). The height of icecap at the location of MICA is 2.7 km above the sea level.

The smallest nadir angle for MICA is  $66.5^\circ$ . About 35% of the neutrinos have the nadir angle in the interval  $66.5^\circ - 70^\circ$ . These neutrinos propagate through the Earth with a maximal depth of 500 km. For  $\eta = 75^\circ$  (where the largest difference of  $A_{ND}$  from CRUST1 and SAW642AN is expected) neutrinos propagate with a maximal depth of 200 km. Neutrinos reach this angle on May 4 for the first time in a year. According to CRUST1 for  $\eta = 75^\circ$ , the depth of Moho is 35 km, with the density jump from 2.9 to  $3.4 \text{ g/cm}^3$ .

In Fig. 9 we show  $A_{ND}(\eta)$  computed with CRUST1 and SAW642AN models. CRUST1 allows to take into account the Earth density above the sea-level. Since

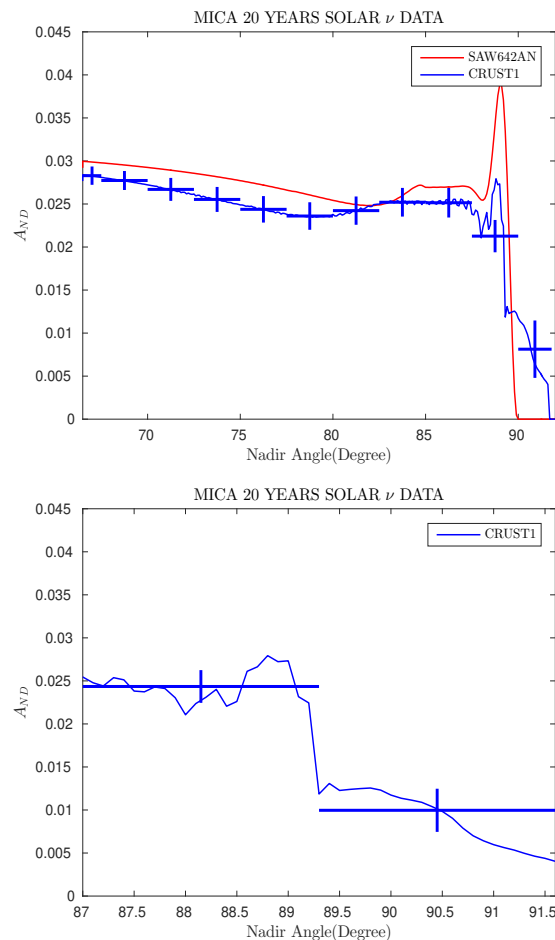


FIG. 9: The Night-Day asymmetry at MICA as function of  $\eta$  for the SAW642AN and CRUST1 models. The crosses present the expected accuracy after twenty years of exposure and taking the CRUST1 model. Bottom panel shows zoomed part of the upper plot for nadir angles larger than  $87^\circ$ . For  $\eta > 89.3^\circ$ , neutrinos cross ice only.

there is no data available for SAW642AN, for this region, we take zero density above the sea-level. After 20 years of data taking MICA will collect  $10^7$  solar neutrino events, and it will be sensitive to the ice-soil border. The average value  $\bar{A}_{ND} = 0.026$  in CRUST1 model can be measured with precision 0.00045. At  $\eta > 89.3^\circ$  neutrinos pass through the ice only, while for smaller  $\eta$  they cross the ice-Earth borderline. The SAW642AN model can be excluded with more than  $4\sigma$ , assuming that CRUST1 is true model. For SAW642AN the only difference of MICA from HK is higher threshold.

Small ripples in  $A_{ND}$  dependence on  $\eta$  that appear in the CRUST model (the blue curve in Fig. 9) are real. In this model the surface of the Earth is not spherically symmetric and the density of the Earth above the sea-level is given. Therefore neutrinos enter the Earth at different height from sea-level, which leads to ripples due

to change of the baseline with  $\eta$ . Such ripples are far from being detected experimentally. The ripples of  $A_{ND}$  are absent in the SAW642AN model (the red curve).

### Dependence on $\Delta m_{21}^2$ ; PREM model results

There is significant difference in values of  $\Delta m_{21}^2$  determined by KAMLAND and from global fit of the solar neutrino data. In this connection we performed computations of  $A_{ND}(\eta)$  using the “solar” value  $\Delta m_{21}^2 = 5 \times 10^{-5} \text{ eV}^2$  (Fig. 10). The changes are twofold: the overall asymmetry increases as  $1/\Delta m_{21}^2$ , *i.e.* becomes 1.5 times larger than before. The oscillation and attenuation lengths increase by the same factor 1.5. This, in turn, leads to (i) some change of the interference picture, (ii) enhancement of sensitivity to remote structures and bigger densities. As a result, at small  $\eta$  enhancement factor of the asymmetry is bigger than than 1.5.

Let us compare results computed for DUNE with the S-R model for two different  $\Delta m_{21}^2$  (blue line in Fig. 10 and black line in Fig. 6). As expected, for large  $\eta$  the amplitude of oscillations of  $A_{ND}$  and its average value are 1.6 times larger than those for large  $\Delta m_{21}^2$ . The dip at  $77^\circ$  disappears. The peak at  $50^\circ$  is higher by factor 1.8. For deeper trajectories (smaller  $\eta$ ) the enhancement factor is 1.80 – 1.85. The reason for this additional increase of the asymmetry above factor 1.5 is that due to larger oscillation length for deep trajectories the effective initial and final densities (averaged over the oscillation length) become larger. For HK and CRUST1 model the results of  $\Delta m_{21}^2$  change are similar: For shallow trajectories the asymmetry increases by factor 1.5, while for deep trajectories (small  $\eta$ ) – by factor 2.

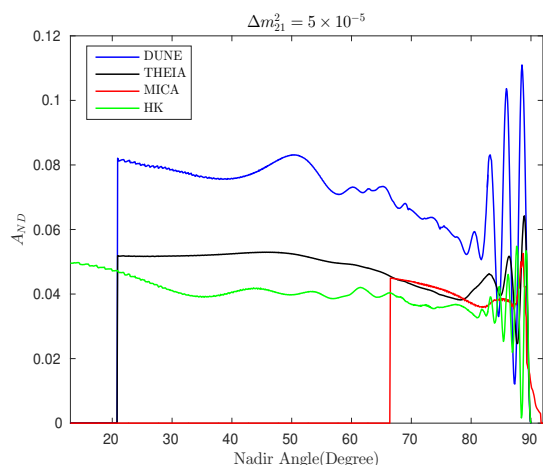


FIG. 10:  $A_{ND}$  for  $\Delta m_{21}^2 = 5 \times 10^{-5} \text{ eV}^2$ . The S-R model was used for DUNE and THEIA while the CRUST1 model – for HK and MICA.

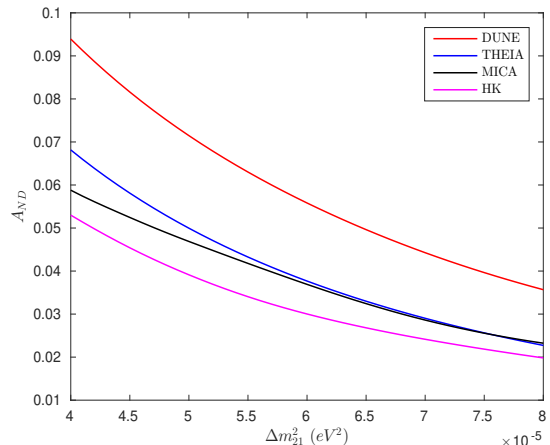


FIG. 11: The averaged over energy  $A_{ND}$  as function of  $\Delta m_{21}^2$  for DUNE and THEIA using the S-R model, and for HK and MICA with CRUST1 model.

Most of the previous computations were performed with PREM model which has two layers in the crust (0 - 15) km and (15 - 24.4) km and density jumps from 2.6 to 2.9  $\text{g/cm}^3$  at 15 km, and 2.9 to 3.38  $\text{g/cm}^3$  at 24.4 km (Moho). The 3 km layer of water is neglected. In Fig. 12 (upper panel) we compare results of PREM (black line) and CRUST1 (blue line) models for DUNE. The difference is mainly related to the depths of Moho:  $\eta_{Moho} = 48 \text{ km}$  for CRUST1, which is two times larger than in PREM. Correspondingly, in the CRUST1 model, the dip of  $A_{ND}$  is shifted to smaller  $\eta$  and for  $\eta < \eta_{dip}$  the asymmetry is smaller. The latter is due to smaller effective density (averaged over the oscillation length) near the detector in CRUST1.

The PREM result is similar to that in [41]. Less profound oscillatory modulations than in [41] are related to different treatment of the energy resolution. As we mentioned before, the PREM model result is close to that of SAW642AN model which has similar depth of Moho.

For comparison in Fig. 12 we show also result for PREM model with outer water layer. That would correspond to a detector near the ocean coast. Large difference appears for  $\eta > 88^\circ$  *i.e.* for trajectories in water: the depth of oscillations and average  $A_{ND}$  are smaller since they correspond to small water density  $1.02 \text{ g/cm}^3$ .

Similar situation is for HK Fig. 12 (bottom). According to CRUST1 the dip is absent,  $A_{ND}$  is larger in the range  $\eta = 75^\circ - 85^\circ$ , while at  $\eta < 75^\circ$  the asymmetry is 10% smaller (by 0.002) than for PREM.

The results show that usage of PREM model causes up-to 10% relative systematic error in  $A_{ND}$ .

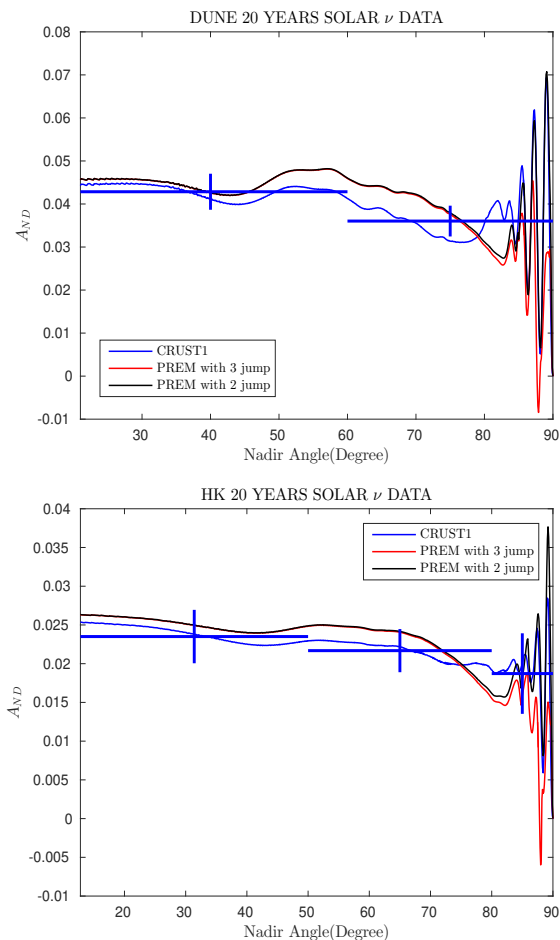


FIG. 12: Comparison of the  $\Delta A_{ND}$  dependences on  $\eta$  computed using the PREM model with two (black line) and three (red) layers in the crust with  $\Delta A_{ND}$  dependence for the CRUST model (blue). *Upper panel:* for DUNE; *bottom panel:* for HyperKamiokande.

## V. CONCLUSION

1. We performed detailed study of the Earth matter effects on solar neutrinos using recent 3D models of the Earth. Interesting and non-trivial oscillation physics is realized which is related to complicated density profiles along neutrino trajectories. The Day-Night asymmetry as a function of the nadir angle has been computed for future experiments DUNE, THEIA and HyperKamiokande, as well as for possible next-after-next generation experiment MICA. This allows us to assess feasibility of tomography of the Earth with solar neutrinos.

2. We estimated corrections to  $A_{ND}$  of the order  $\sim \epsilon^2$ . Corrections  $\sim \epsilon^2$  from  $I_2$  can be neglected due to additional small coefficient, while the  $\epsilon$  correction to the oscillation phase can be relevant.

3. We further elaborated on the attenuation effect.

The night excess of events and  $A_{ND}(\eta)$  are expressed in terms of the matter potential and the generalized energy resolution function which, in turn, determines the attenuation factor. This form is the most appropriate for tomography. We have found that inclusion of energy dependence of the boron neutrino flux and cross-section into resolution function improves the resolution, and therefore sensitivity to remote structures. It is the generalized resolution function that determines sensitivity of oscillation results to the density profile.

Further improvement of the sensitivity can be achieved imposing high enough energy threshold for detected electrons. The gain is twofold: (i) The Earth matter effect increases as  $E$ ; (ii) the attenuation becomes weaker. At the same time loss of statistics is rather moderate.

4. Using recently elaborated 3D models of the Earth we reconstructed the density, and consequently, potential profiles along neutrino trajectories characterized by coordinates of a detector, nadir and azimuthal angles. The key feature of the models is the absence of spherical symmetry. Averaging over  $\phi_a$  leads to dumping of oscillatory modulations.

The key feature of profiles that determines the  $A_{ND}(\eta)$  is the depth of Moho (border between crust and mantle). The depth differs substantially in different models, and furthermore the border substantially deviates from spherical form.

5. Difference of results for different models of the Earth at DUNE and THEIA at Homestake is about 10%. After 20 years of DUNE exposure that would correspond to  $1\sigma$ . So, the models cannot be discriminated. Similar conclusion is valid for HK.

6. MICA will be sensitive to the ice-soil border. It can discriminate between the CRUST1 and SAW642AN models at  $4\sigma$  C.L. after 20 years of data taking.

7. With decrease of  $\Delta m_{21}^2$  the overall excess increases as  $1/\Delta m_{21}^2$ . Also  $\eta$  dependence changes which is related to increase of the oscillation length and therefore decrease of the oscillation phase: for deep trajectories the enhancement with decrease of  $\Delta m_{21}^2$  is stronger than  $1/\Delta m_{21}^2$ .

8. The difference of results obtained for Homestake with S-R and CRUST1 from those of PREM model, which was used in most of previous studies, is that the dip in the nadir angle distribution does not appear and for deep trajectories the asymmetry is 10% lower.

In conclusion, future experiment DUNE, THEIA, HK will certainly establish the integrated Earth matter effect with high significance. They may observe some generic features of the  $\eta$  dependence such as dip and slow increase of the excess with decrease of  $\eta$ . However, they will not be able to discriminate between recent models. For this megaton scale experiments like MICA are needed.

### Acknowledgments

P.B. would like to thank M. Rajaei, M. Bahraminasr and M. Maltoni for useful discussions. P.B. received funding from the European Unions Horizon 2020 research and innovation programme under the Marie Skłodowska-Curie Grant Agreement No. 674896 and No. 690575. P.B. is supported by Iran Science Elites Federation Grant No. 11131. P.B. thanks MPIK and IFT for their kind hospitality and support.

### Appendix A. Neutrino Trajectory in the Earth

The Earth can be considered as a sphere with a very small compared to the Earth radius deviations from the sphere. So, the distance of a given point at the surface from the centre of the Earth equals  $r_E(\theta, \phi) = 6371 \text{ km} + H(\theta, \phi)$ , where  $H(\theta, \phi)$  is the height from the sea-level of the location. Here,  $\theta$  and  $\phi$  are the latitude and longitude of the point respectively. Let us introduce coordinates  $x$ ,  $y$  in the plane perpendicular to the axis of rotation of the Earth and  $z$  being along the axis. The axis is tilted by about  $\alpha = 23.4^\circ$  relative to the Earth orbital plane. In these coordinates location of a point on the Earth surface at a given moment of time  $t$  is determined by

$$\begin{aligned} x &= r_E(\theta, \phi) \cos \theta \cos(\phi + \omega t), \\ y &= r_E(\theta, \phi) \cos \theta \sin(\phi + \omega t) \cos \alpha - r_E(\theta, \phi) \sin \alpha \sin \theta, \\ z &= r_E(\theta, \phi) \sin \theta \cos \alpha + r_E(\theta, \phi) \cos \theta \sin(\phi + \omega t) \sin \alpha, \end{aligned} \quad (52)$$

where  $\omega$  is the angular frequency of the Earth rotation.

Location (latitude and longitude) of DUNE, THEIA (Homestake) is  $44.35^\circ$  of north and  $103.75^\circ$  of the west. For H-Kamiokande (Hida) we have  $36.23^\circ$  of north and  $137.19^\circ$  of the east, and for MICA (Amundsen-Scott South Pole Station):  $89.99^\circ$  south and  $63.45^\circ$  west.

In all the cases except for MICA we have considered the Earth surface as a perfect sphere ( $H(\theta, \phi) = 0$ ), and the detectors located at the surface of the Earth. In the case of MICA, we used CRUST1 model, which allow to take into account  $H(\theta, \phi)$ , and the detector is location  $2.25 \text{ km}$  below the ice surface.

The coordinates of the Earth in the solar system are

$$X = r_a \cos(\Omega t + \Phi_0), \quad Y = r_a \sin(\Omega t + \Phi_0), \quad (53)$$

where  $\Omega$  is  $2\pi/(365.256 \text{ days})$ , and  $r_a = a(1 - b \cos \Omega t)$  is the distance between Earth and Sun. Here  $a=1$  is the astronomical unit, and  $b=0.0167$  is the eccentricity of the Earth orbit. For the starting point,  $t = 0$ , at the 23rd of September the phase equals  $\Phi_0 = -\frac{\pi}{2}$ .

Let  $x_D$  and  $y_D$  be the coordinates of the detector and  $x$ ,  $y$  and  $z$  are the coordinates of the point at which neutrino enters the Earth. The neutrino trajectory inside the

Earth is determined by solving the following quadratic equation:

$$x^2 + y^2 = r_D^2, \quad y = m(x - x_D) + y_D, \quad (54)$$

where  $m \equiv Y/X$  and  $r_D^2 = x_D^2 + y_D^2$ . Taking into account tilt  $\alpha$ , the latitude and longitude of the entering point to the Earth and consequently, the trajectory of the neutrino inside the Earth as well as the nadir angle are determined.

To perform a precise calculation of the neutrino trajectory for MICA we use the CRUST1 model. In this case, the Earth is not a perfect sphere. Therefore we solved the quadratic equation first with  $r_E$  that includes  $H_d$  the depth of the detector from the sea-level. In this way, we obtained the entrance point of the neutrinos into the Earth,  $\theta_0$  and  $\phi_0$ . Then we have solved Eq. (54) once again with  $H(\theta_0, \phi_0)$ .

### References

- 
- [1] S. P. Mikheyev and A. Yu. Smirnov, Proc. of the 6th Moriond Workshop on massive Neutrinos in Astrophysics and Particle Physics, Tignes, Savoie, France Jan. 1986 (eds. O. Fackler and J. Tran Thanh Van) p. 355 (1986).
  - [2] E. D. Carlson, Phys. Rev. D **34** (1986) 1454.
  - [3] M. Cribier, W. Hampel, J. Rich and D. Vignaud, Phys. Lett. B **182** (1986) 89.
  - [4] J. Bouchez, M. Cribier, J. Rich, M. Spiro, D. Vignaud and W. Hampel, Z. Phys. C **32** (1986) 499.
  - [5] S. Hiroi, H. Sakuma, T. Yanagida and M. Yoshimura, Prog. Theor. Phys. **78** (1987) 1428.
  - [6] A. J. Baltz and J. Weneser, Phys. Rev. D **35** (1987) 528.
  - [7] A. Dar, A. Mann, Y. Melina and D. Zajfman, Phys. Rev. D **35** (1987) 3607.
  - [8] S. P. Mikheyev and A. Yu. Smirnov, Proc. of 7th Moriond Workshop on Search for New and Exotic Phenomena, Les Arcs, Savoie, France, 1987, edited by O. Fackler and J. Tran Thanh Van (Editions Frontieres, Gif-sur-Yvette, France, 1987) p. 405.
  - [9] A. J. Baltz and J. Weneser, Phys. Rev. D **37** (1988) 3364.
  - [10] A. J. Baltz and J. Weneser, Phys. Rev. D **51** (1995) 3960.
  - [11] E. Lisi and D. Montanino, Phys. Rev. D **56** (1997) 1792 [hep-ph/9702343].
  - [12] Q. Y. Liu, M. Maris and S. T. Petcov, Phys. Rev. D **56** (1997) 5991 [hep-ph/9702361].
  - [13] M. Maris and S. T. Petcov, Phys. Rev. D **56** (1997) 7444 [hep-ph/9705392].
  - [14] Y. Fukuda *et al.* [Super-Kamiokande Collaboration], Phys. Rev. Lett. **82** (1999) 1810 [hep-ex/9812009].
  - [15] A. Dighe, Q. Y. Liu and A. Y. Smirnov, hep-ph/9903329.
  - [16] A. de Gouvea, A. Friedland and H. Murayama, JHEP **0103** (2001) 009 [hep-ph/9910286].
  - [17] J. S. Kim and K. Lee, Comput. Phys. Commun. **135** (2001) 176 [hep-ph/0006137].
  - [18] G. L. Fogli, E. Lisi, D. Montanino and A. Palazzo, Phys. Rev. D **62** (2000) 113003 [hep-ph/0008012].

- [19] C. W. Chiang and L. Wolfenstein, *Phys. Rev. D* **63** (2001) 057303 [hep-ph/0010213].
- [20] M. C. Gonzalez-Garcia, C. Pena-Garay and A. Y. Smirnov, *Phys. Rev. D* **63** (2001) 113004 [hep-ph/0012313].
- [21] M. Maris and S. T. Petcov, *Phys. Lett. B* **534** (2002) 17 [hep-ph/0201087].
- [22] A. N. Ioannisian and A. Y. Smirnov, hep-ph/0201012.  
M. Blennow, T. Ohlsson and H. Snellman, *Phys. Rev. D* **69** (2004) 073006 [hep-ph/0311098].
- [23] M. B. Smy *et al.* [Super-Kamiokande Collaboration], *Phys. Rev. D* **69** (2004) 011104 [hep-ex/0309011].
- [24] A. N. Ioannisian and A. Y. Smirnov, *Phys. Rev. Lett.* **93** (2004) 241801 [hep-ph/0404060].
- [25] E. K. Akhmedov, M. A. Tortola and J. W. F. Valle, *JHEP* **0405** (2004) 057 [hep-ph/0404083].
- [26] A. N. Ioannisian, N. A. Kazarian, A. Y. Smirnov and D. Wyler, *Phys. Rev. D* **71** (2005) 033006 [hep-ph/0407138].
- [27] J. Hosaka *et al.* [Super-Kamiokande Collaboration], *Phys. Rev. D* **73** (2006) 112001 [hep-ex/0508053].
- [28] M. Wurm *et al.*, *Phys. Rev. D* **83** (2011) 032010 [arXiv:1012.3021 [astro-ph.IM]].
- [29] A. Renshaw *et al.* [Super-Kamiokande Collaboration], *Phys. Rev. Lett.* **112** (2014) no.9, 091805 [arXiv:1312.5176 [hep-ex]].
- [30] S. S. Aleshin, O. G. Kharlanov and A. E. Lobanov, *Phys. Rev. D* **87** (2013) no.4, 045025 [arXiv:1302.7201 [hep-ph]].
- [31] O. G. Kharlanov, arXiv:1509.08073 [hep-ph].
- [32] A. N. Ioannisian and A. Y. Smirnov, *Phys. Rev. D* **96** (2017) no.8, 083009 [arXiv:1705.04252 [hep-ph]].
- [33] A. M. Dziewonski and D. L. Anderson, *Phys. Earth Planet. Interiors* **25** (1981) 297.
- [34] R. Acciarri *et al.* [DUNE Collaboration], arXiv:1512.06148 [physics.ins-det].
- [35] [Hyper-Kamiokande Collaboration], KEK-PREPRINT-2016-21, ICRR-REPORT-701-2016-1.
- [36] J. R. Alonso *et al.*, arXiv:1409.5864 [physics.ins-det].
- [37] M. Askins *et al.* [Theia Collaboration], arXiv:1911.03501 [physics.ins-det].
- [38] S. Boser, M. Kowalski, L. Schulte, N. L. Strotjohann and M. Voge, *Astropart. Phys.* **62** (2015) 54 [arXiv:1304.2553 [astro-ph.IM]].
- [39] D. Adey *et al.* [Daya Bay Collaboration], *Phys. Rev. Lett.* **121** (2018) no.24, 241805 [arXiv:1809.02261 [hep-ex]].
- [40] J. N. Bahcall, E. Lisi, D. E. Alburger, L. De Braeckeleer, S. J. Freedman and J. Napolitano, *Phys. Rev. C* **54** (1996) 411 [nucl-th/9601044].
- [41] A. Ioannisian, A. Smirnov and D. Wyler, *Phys. Rev. D* **96** (2017) no.3, 036005 [arXiv:1702.06097 [hep-ph]].
- [42] Shen, W. & Ritzwoller, M.H., 2016. Crustal and uppermost mantle structure beneath the United States, *J. geophys. Res.*
- [43] Tao K., Grand S. P. and Niu F. N. (2018), Seismic structure of the upper mantle beneath Eastern Asia from full waveform seismic tomography, *Geochemistry, Geophysics, Geosystems* 10.1029/2018GC007460.
- [44] Megnin, Charles and Barbara Romanowicz. 2000. The shear velocity structure of the mantle from the inversion of of body, surface and higher modes waveforms., *Geophys. J. Int.* 143:709-728.
- [45] Laske, G., Masters, G., Ma, Z. and Pasyanos, M., Update on CRUST1.0 - A 1-degree Global Model of Earth's Crust, *Geophys. Res. Abstracts*, 15, Abstract EGU2013-2658, 2013.
- [46] James Stewart Monroe; Reed Wicander (2008). *The changing Earth: exploring geology and evolution* (5th ed.). Cengage Learning. p. 216. ISBN 978-0-495-55480-6.
- [47] Benjamin Franklin Howell (1990). *An introduction to seismological research: history and development*. Cambridge University Press. ISBN 0-521-38571-7.
- [48] Tenzer, R., Bagherbandi, M., 2013. Reference crust-mantle density contrast beneath Antarctica based on the Vening Meinesz Moritz isostatic problem and CRUST2.0 seismic model. *Earth. Sci. Res. J.* 17, 1, 712.
- [49] If for high energy Boron neutrinos the background is negligible, all the events can be considered as being due to solar neutrinos. In this case, the study may be performed on an event-by-event basis and not on a statistical basis. The neutrino energy can be reconstructed measuring the energy and direction of the recoil electron with respect to the direction to the Sun. In this case, the analysis described for the neutrino-nuclei interactions is valid although the reconstruction function is expected to be wider.